

Effects of Using High Resolution Satellite-based Inundation Time Series to Estimate Methane Fluxes from Forested Wetlands

Kelly Hondula¹, Ben DeVries², C. Nathan Jones³, and Margaret A. Palmer⁴

¹University of Maryland, College Park

²University of Guelph

³University of Alabama

⁴University of Maryland Center For Environmental Sciences

November 22, 2022

Abstract

A major source of uncertainty in the global methane budget arises from quantifying the area of wetlands and other inland waters. This study addresses how the dynamics of surface water extent in forested wetlands affect the calculation of methane emissions. We used fine resolution satellite imagery acquired at sub-weekly intervals together with a semi-empirical methane emissions model to estimate daily surface water extent and diffusive methane fluxes for a low-relief wetland-rich watershed. Comparisons of surface water model predictions to field measurements showed agreement with the magnitude of changes in water extent, including for wetlands with surface area less than 1,000 m². Results of methane emission models showed that wetlands smaller than 1 hectare (10,000 m²) were responsible for a majority of emissions, and that considering dynamic inundation of forested wetlands resulted in 49–62% lower emission totals compared to models using a single estimate for each wetland's size.

Hosted file

hondula-gr1-resubmission-supplemental.docx available at <https://authorea.com/users/541026/articles/600412-effects-of-using-high-resolution-satellite-based-inundation-time-series-to-estimate-methane-fluxes-from-forested-wetlands>

1
2
3
4
5
6
7
8
9
10
11
12
13
14
15
16
17
18

Effects of Using High Resolution Satellite-based Inundation Time Series to Estimate Methane Fluxes from Forested Wetlands

Kelly L. Hondula¹, Ben DeVries², C. Nathan Jones³, and Margaret A. Palmer¹

¹National Socio-Environmental Synthesis Center, University of Maryland, MD, USA.
²Department of Geography, Environment and Geomatics, University of Guelph, Ontario, Canada. ³Department of Biological Sciences, University of Alabama, AL, USA.

Corresponding author: Kelly Hondula (kellyhondula@gmail.com)

Key Points:

- Variable inundation extent in forested wetlands has large implications for calculating methane emissions.
- Surface water maps based on 30m imagery likely exclude wetlands that contribute a majority of methane emissions from forested landscapes.
- High resolution optical imagery underestimates surface water extent in forested wetland landscapes during periods of high canopy cover.

19 **Abstract**

20 A major source of uncertainty in the global methane budget arises from quantifying the area of
21 wetlands and other inland waters. This study addresses how the dynamics of surface water extent
22 in forested wetlands affect the calculation of methane emissions. We used fine resolution satellite
23 imagery acquired at sub-weekly intervals together with a semi-empirical methane emissions
24 model to estimate daily surface water extent and diffusive methane fluxes for a low-relief
25 wetland-rich watershed. Comparisons of surface water model predictions to field measurements
26 showed agreement with the magnitude of changes in water extent, including for wetlands with
27 surface area less than 1,000 m². Results of methane emission models showed that wetlands
28 smaller than 1 hectare (10,000 m²) were responsible for a majority of emissions, and that
29 considering dynamic inundation of forested wetlands resulted in 49–62% lower emission totals
30 compared to models using a single estimate for each wetland's size.

31

32 **Plain Language Summary**

33 Wetlands and small ponds are hotspots for greenhouse gas emissions, especially methane.
34 Quantifying how much, though, depends on accurately mapping each of those water bodies.
35 Whereas most medium and large lakes are visible to satellites, smaller bodies are generally
36 missing from the best maps and flooded areas in forests are overlooked. Additionally, many of
37 these systems change in size depending on the current season and rainfall patterns. We use
38 several hundred high resolution satellite images collected over the same forested region over the
39 course of one year to estimate how much water bodies changed in size, and the subsequent effect
40 that has on methane emissions from this area. We found that wetlands only visible in high
41 resolution imagery were responsible for most of the total methane emissions, and that accounting
42 for changing wetland size throughout the year halved the estimated emissions.

43 **1 Introduction**

44 Global change is affecting the quantity, quality, and timing of material fluxes through
45 ecosystems with consequences for the fate and transformation of carbon. Inland waters are now
46 recognized as fundamental to understanding the global carbon (C) cycle (Cole et al., 2007;
47 Raymond et al., 2013; Tranvik et al., 2009) yet our ability to characterize C fluxes and their
48 drivers at landscape and regional scales remains limited by available data on surface water extent
49 (SWE) and dynamics—particularly for forested wetlands, very small water bodies (e.g. ponds),
50 and areas with temporally varying inundation. Collectively, these limitations represent a major
51 shortcoming in our ability to account for methane emission sources, and at least one third of all
52 uncertainty in the global methane budget (Melton et al., 2013; Saunio et al., 2020).

53 Methane emissions for lakes, ponds, reservoirs, streams, and rivers have been calculated
54 by upscaling the best available data on flux rates and the areal extent of those waters by category
55 (Saunio et al., 2020). However, for wetlands, a combination of land cover maps, remote sensing
56 data, and simulated hydrologic fluxes are used to calculate temporally varying methane
57 producing areas as inputs to process-based biogeochemical models (Poulter et al., 2017; Wania
58 et al., 2012). Both approaches suffer from uncertainties associated with spatial and temporal
59 variation in inundation extent which is highly relevant for resolving sources and sinks of
60 methane at global scales. This wetland extent problem contributes substantial uncertainty in

61 methane budgets and limits our ability to identify drivers of recent increases in atmospheric
62 concentrations (Thornton et al., 2016).

63 Upscaling empirical data on gas flux rates to quantify freshwater methane emissions is
64 fraught with biases, including inadequate representation of underlying drivers (DeSontro et al.,
65 2018; Seekell et al., 2014) and lack of consideration of seasonal events such as ice-out or non-
66 growing season emissions (Treat et al., 2018). Despite advances in remote sensing of aquatic
67 systems, identifying small water bodies remains a challenge because they are often optically
68 complex, obscured by vegetation, or below the resolvable size of satellite sensors (Allen &
69 Pavelsky, 2018; Kuhn et al., 2019). The resulting omission of forested wetlands, small water
70 bodies, and inundation dynamics in land cover and surface water data sets is broadly recognized
71 (DeVries et al., 2017; Lang et al., 2020), but its implications for methane emissions accounting is
72 unresolved (Poulter et al., 2017; Thornton et al., 2016). This is despite recognition that
73 headwaters and small water bodies play disproportionate roles in ecosystem processes (Hanson
74 et al., 2007; Holgerson & Raymond, 2016; Lowe & Likens, 2005) and may comprise the largest
75 proportion of freshwater area (Bishop et al., 2008; Downing et al., 2006).

76 The ability to monitor and detect surface water at higher spatial and temporal resolution
77 is advancing through new technologies including sub-pixel methods (DeVries et al., 2017),
78 fusion with hydrologic models (Evenson, Golden, et al., 2018), satellite constellations (Claverie
79 et al., 2018; Cooley et al., 2019), and applications of machine learning (Jia et al., 2018; Lang et
80 al., 2020; Lee et al., 2019). However, most remote sensing applications for freshwater bodies
81 remain focused on relatively large or unvegetated systems (Griffin et al., 2018; Kuhn et al.,
82 2019; Pekel et al., 2016) by excluding pixels influenced by fractional coverage of soil and
83 vegetation (Ji et al., 2009). Using such methods is warranted to avoid classification errors
84 associated with spectral unmixing (Halabisky et al., 2016), but it can also result in large
85 uncertainties for C fluxes at regional or global scales (Melton et al., 2013; Thornton et al., 2016;
86 Treat et al., 2018) due to substantial underrepresentation of SWE (DeVries et al., 2017). Previous
87 studies have explored inter-annual variability in wetland extent (Huang et al., 2014; Lang et al.,
88 2020; Yeo et al., 2019) but investigation of intra-annual dynamics has generally been limited by
89 availability of cloud-free leaf-off imagery. Further, most investigations have not characterized
90 inundation patterns for individual wetlands (Vanderhoof et al., 2018) or used sub-pixel
91 estimation techniques (DeVries et al., 2017; Yeo et al., 2019) to account for the preponderance
92 of small water bodies that result in mixed spectral signatures for pixels in 30 m resolution
93 imagery.

94 Discrepancies between top-down and bottom-up emissions tend to be largest from
95 forested areas (Melton et al., 2013). Recent investigations into these discrepancies have
96 uncovered new sources and emission pathways from trees (Pangala et al., 2017). Further, in
97 tropical regions, wetland emission models underestimate emissions compared to observations
98 with the largest discrepancy in years with significant wetland flooding (Parker et al., 2018).
99 Because surface water maps exclude most under-canopy inundation, evasion from these
100 inundated regions may also play an important role in explaining emissions from seasonally
101 dynamic temperate forested areas that are not reproduced in existing wetland models.

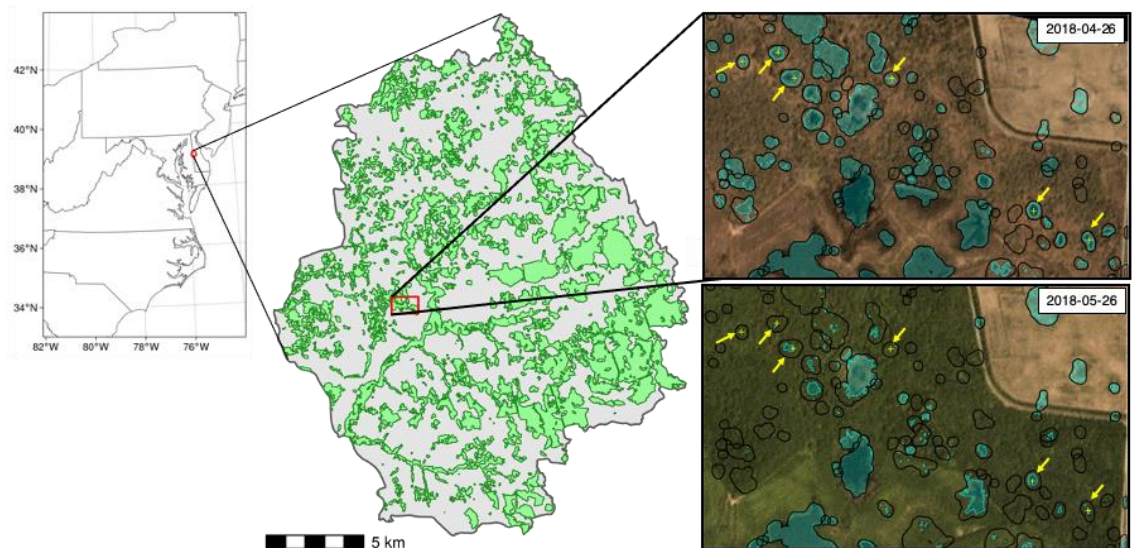
102 This study was designed to fill gaps in our understanding of how forested wetland size
103 and temporal variation in inundation influence watershed-scale estimates of methane emissions.
104 We combine elements from both the wetland and inland water calculation approaches described

105 above to estimate one year of diffusive methane emissions from forested wetlands across a 347
 106 km² mid-Atlantic Coastal Plain watershed. We use fine resolution frequent-repeat remote sensing
 107 imagery to estimate daily SWE at the wetland scale as input to field-validated semi-empirical
 108 models for calculating methane emissions. As in other studies, we assume SWE is a proxy for
 109 methane producing area. Results demonstrate that i) excluding inundation variability increased
 110 modeled methane emission totals by 66–105%, but ii) excluding small water bodies (< 1,000 m²)
 111 reduced inundation estimates and subsequent emissions by 30% and 38–51%.

112 2 Methodology

113 2.1 Study area

114 Our study site, the 347 km² Greensboro watershed, is on the Delmarva Peninsula
 115 (Maryland, USA), a low-gradient coastal plain landscape defined by poorly drained soils and the
 116 persistence of small depressional forested wetlands surrounded by extensive ditch-drained
 117 agricultural land (Figure 1; Jones et al., 2018). Known as Delmarva Bays, these wetlands range
 118 in size from small closed canopy wetlands (<0.5 ha; similar to vernal pools in the northeast) to
 119 large open canopy wetlands (>5 ha; similar to Carolina Bays) (Phillips & Shedlock, 1993).
 120 Typically they dry seasonally, having maximum inundation during the winter and decreasing
 121 water levels through the spring and summer due to evapotranspiration and agricultural
 122 groundwater withdrawal (Lee et al., 2020).

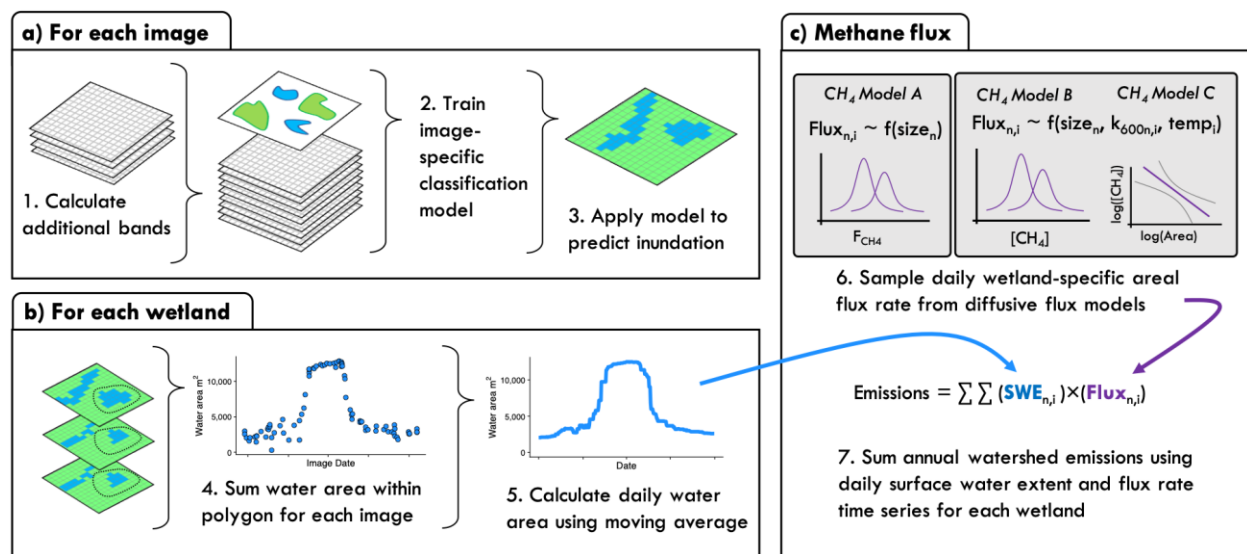


123
 124 **Figure 1.** Study area showing location of the Greensboro watershed and forested wetlands.
 125 Wetland boundaries, monitoring locations, and surface water classification model predictions for
 126 2 images are shown over corresponding color-corrected PlanetScope Visual Ortho Scenes
 127 (Planet, 2018).

128 Draining to the Chesapeake Bay via the Choptank River, this watershed has been the
 129 focal point for extensive research (e.g., Ator & Denver, 2012). Land cover is mainly cultivated
 130 crops (50.5%), woody wetlands (31.5%), and deciduous forest 7.7% (Jin et al., 2019). We define
 131 wetlands using a previously developed dataset of topographic depressions (Vanderhoof & Lang,

132 2017) that were derived using the Stochastic Depression Analysis Tool (Lindsay, 2016; Wu et
 133 al., 2014) and filtered using a minimum size of 50 m² and SWE classified from April 2015
 134 Worldview 3 imagery (Vanderhoof et al., 2018). Polygons generally co-occur with features in
 135 the National Wetlands Inventory (NWI) but they are more numerous, cover less total area, and
 136 are more spatially aligned with SWE. We subset this dataset to only those within woody
 137 wetlands land cover using the 2016 National Land Cover Database (NLCD; Jin et al., 2019).
 138 This approach resulted in 5,118 forested wetland depressions (46% of those in the watershed),
 139 which we refer to as focal wetlands.

140 2.2 Remote sensing for surface water classification



141

142 **Figure 2.** Image classification and emissions model workflow. **a)** Image-specific supervised
 143 classification models developed using original 4 bands (R, G, B, NIR) and derived indices
 144 NDVI, NDWI, saturation, chroma, and luminescence; **b)** Daily surface water time series derived for
 145 each focal wetland from predicted surface water area within each polygon boundary across all
 146 images; **c)** Methane emissions for each wetland (*n*) on day (*i*) derived using semi-empirical
 147 models to produce annual estimates of basin-wide emissions.

148 Daily time series of SWE for each focal wetland were calculated using 3 m resolution
 149 PlanetScope imagery (Figure 2; Text S1; Planet, 2018). We downloaded 421 PlanetScope 4-band
 150 images that overlapped the study watershed and had less than 1% cloud cover. These were taken
 151 across 98 days in the 2018 water year, during which wetland surface water levels were monitored
 152 in the field. All images were Surface Reflectance products, which were atmospherically
 153 corrected using the 6SV2.1 radiative transfer model (Planet, 2018; Vermote et al., 1997). Images
 154 were masked to exclude low quality pixels indicated by the unusable data mask provided with
 155 each image. Then, we calculated a suite of spectral indices from the four bands in each image,
 156 including NDWI (McFeeters, 1996), NDVI (Tucker, 1979), saturation, luminescence, and
 157 chroma (Zeileis et al., 2019), resulting in 9 variables for each pixel.

158 Training data for surface water and non-water classes were based on the NWI, the 2016
 159 NLCD, and the wetland depressions dataset developed by (Vanderhoof & Lang, 2017). We

160 defined surface water as Freshwater Pond ($n = 655$) and Lake ($n = 1$) classes in NWI, which are
161 classified in NWI as permanently (99%) or semi-permanently (1%) flooded. We defined non-
162 water areas using NLCD forest and forested wetland classes minus pixels falling within 10m of
163 any NWI polygons or topographic depressions. For each image, pixel values for the 9 bands in
164 the training regions were extracted and a sample was used to train a random forest model that
165 was then applied to the image.

166 For each classified image, we extracted pixel values within a 10m buffer around each
167 focal wetland to calculate the predicted inundation area (Figure 2b). We used the buffer to
168 account for the 10m geolocation uncertainty in the optical data (Planet, 2018), as well as
169 potential expansion of inundation beyond topographic spill points, as is common in this
170 landscape (Jones et al., 2018). Average time between usable images of each focal wetland was 6
171 days, resulting in a time series with 50-102 predictions across the year for each focal wetland.
172 Average maximum time between consecutive usable images was 32 days but ranged up to 74
173 days. We converted the irregularly spaced predictions into a daily time series for each focal
174 wetland using a 50-day rolling median. Time series with gaps longer than 50 days (1%) were
175 excluded from total inundated surface area.

176 2.3 Field measurements

177 For comparison to areal extent of surface water estimated from remote sensing imagery,
178 SWE was measured in the field at 6 wetlands in the study region (Figure 1). Water level was
179 monitored in surface water wells at each wetland center using pressure transducers (Onset
180 HOBO U20L level loggers) recording every 15 minutes. We calculated a daily time series of
181 inundation extent for each wetland using binary classification of a 1m LiDAR-based digital
182 elevation model (Lang et al., 2012) using mean daily water level with a raster-based approach
183 similar to Jones et al., (2018). Estimates were validated using monthly observations of water
184 extent along a fixed transect at each wetland as well as surveys around the perimeter of
185 maximum observed inundation extent in mid-March 2018.

186 2.4 Methane emissions model

187 Daily diffusive methane emissions were calculated using wetland-specific flux rates and
188 predicted daily SWE time series from the random forest classification models (Figure 2c). We
189 developed three models (hereafter referred to as models A, B and C) using variations of a semi-
190 empirical flux rate equation based on the synthesized global dataset of methane concentrations
191 described by Holgerson and Raymond (2016) and validated with field measurements at 6
192 wetlands in the study area (Text S2). Model A predicted daily flux rates by sampling the
193 lognormal distribution of the appropriate logarithmic size class for each wetland. For models B
194 and C, daily flux rates for each wetland [n] were determined using Equation 1 with daily air
195 temperature and atmospheric pressure from a nearby weather station to calculate gas exchange
196 rates and equilibration concentrations of 1.85 ppm atmospheric methane for each day [i]
197 (Winslow et al., 2016). $C_{aq[n]}$ is a time-invariant methane concentration for each wetland [n]

198 based on its size. Gas exchange rates were calculated using daily temperature values and the
199 size-class specific k_{600} values described in Holgerson and Raymond (2016).

200 Equation 1: $Flux_{n,i} = k_{n,i} \times (C_{aq[n]} - C_{eq[i]})$

201 For model B, $C_{aq[n]}$ was randomly sampled from a lognormal distribution based on the
202 size class of each focal wetland's original area, and for model C, $C_{aq[n]}$ was predicted from the
203 area-concentration regression model. Because forested wetlands are a high outlier for methane
204 on the relationship between water body size and methane concentration reported by Holgerson
205 and Raymond (2016), our calculated emissions are likely a conservative estimate. We estimated
206 flux rate uncertainty using Monte Carlo resampling to generate a distribution of emission
207 estimates for each wetland by running each model 1,000 times. Cumulative annual emissions
208 across all wetlands were calculated using Equation 2, where $SWE_{[n,i]}$ is the SWE of depression
209 [n] on day [i] calculated from the classification model time series.

210 Equation 2: $Total\ Emissions = \sum \sum Flux_{n,i} \times SWE_{n,i}$

211 We evaluated the effects of different model assumptions by calculating total annual
212 methane emissions under each model with and without changes in SWE, based on the original
213 area of each focal wetland. Models accounting for changes in SWE we call dynamic area
214 models; models not accounting for these we call static area models.

215 **3 Results**

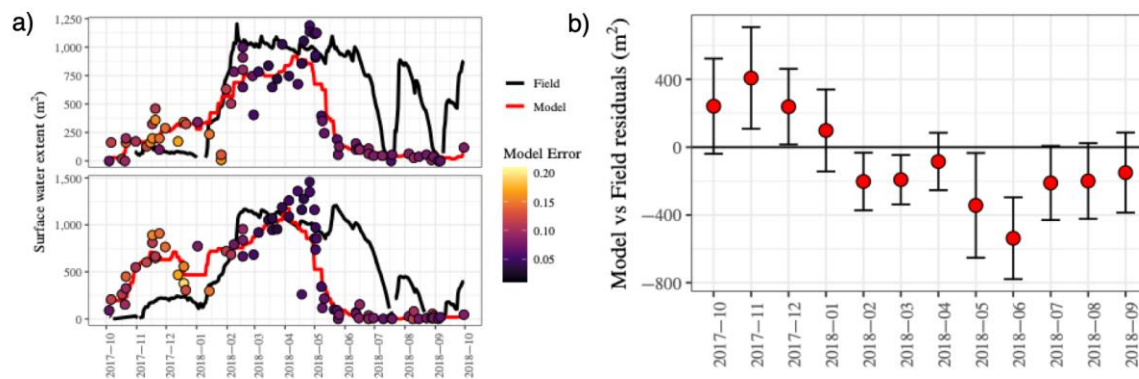
216 3.1 Magnitude and variability of predicted SWE

217 Total predicted SWE within focal forested wetlands across the watershed ranged from a
218 low of 1.3 km² in late July to 6.2 km² in early April, with an average of 3.75 km². This area was
219 an order of magnitude higher than maximum extent reported for the watershed in the global
220 surface water area database (0.70 km²; (Pekel et al., 2016)) and represents 2.5-5.7% of the entire
221 watershed area, 50-113% of the area of topographic depressions, and 10-23% of the total area of
222 NWI palustrine wetlands (U. S. Fish and Wildlife Service, 2019).

223 3.2 Classification model performance

224 Classification models were sufficiently able to discriminate between water and non-water
225 areas. Comparisons between field-based and satellite-based inundation time series show that our
226 modeling approach was able to quantify the magnitude of seasonal changes in SWE for
227 individual wetlands, even for those smaller than 1,000 m². For the field-monitored wetlands, the
228 maximum predicted extent and range from classification models were significantly related to
229 observed values ($\rho = 0.91$, $\rho = 0.83$, respectively; $\alpha = 0.05$). However, the models consistently
230 underpredicted May and June 2018 SWEs and overestimated November 2017 SWE (Figure 3).
231 Monthly averaged residuals between field and satellite-based wetland areas were largest during
232 these two periods (Figure 3b), but only in autumn 2017 was model accuracy also low (Figure

233 3a). The Nash-Sutcliffe (NSC) criteria to evaluate model efficiency indicated poor fit (NSE <0.5)
 234 between the daily simulated and observed water extents.



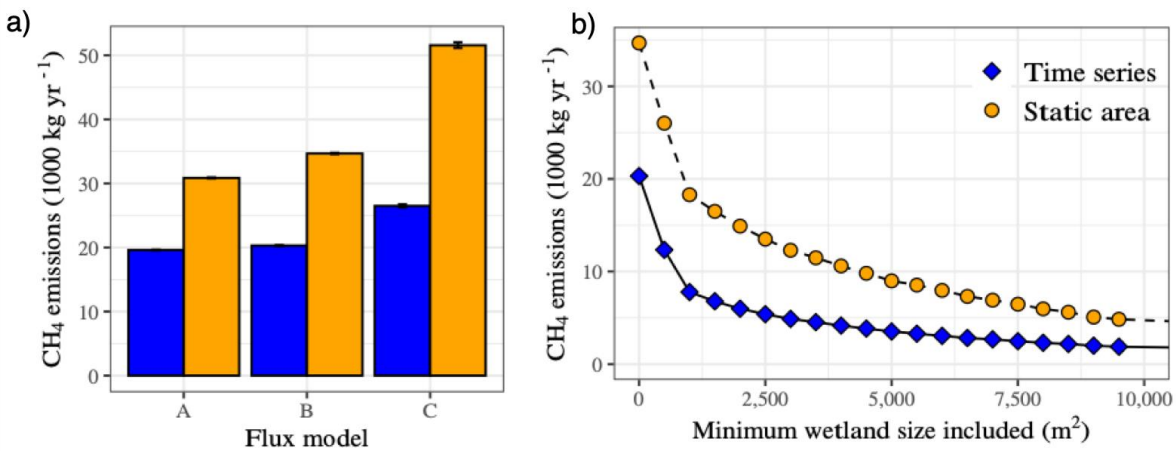
235

236 **Figure 3.** Comparison between inundation time series developed from field monitoring and
 237 satellite data. **a)** Inundation time series from two wetlands comparing field data and predictions
 238 from image-based classification models, along with estimates from individual images (points)
 239 shaded by model error rate. **b)** Average monthly residuals (\pm sd) between model predictions of
 240 SWE from image classification and field data for all observations across the 6 wetlands with
 241 field water level data.

242 3.3 Methane emission totals under different model assumptions

243 Calculating watershed methane emissions using a time series approach to quantify
 244 variation in surface water coverage resulted in total estimated annual emissions 49-62% lower
 245 than when static wetland sizes were used (Figure 4a). Using the concentration-area regression
 246 flux model (C) resulted in higher emission totals than either the size category flux (A) or size
 247 category concentration (B) models, but in all three cases the difference between the dynamic and
 248 static models was substantially greater than variability associated with methane flux rate
 249 uncertainty. We also observed that small wetlands (< 1 ha) were responsible for a considerable
 250 proportion of modeled emissions. Although the static area models overestimated emissions for
 251 any given minimum wetland size threshold, they are only overestimates compared to the best
 252 estimate of total emissions if wetlands smaller than 1,000 m² are included. Excluding these

253 resulted in an underestimate of total emissions by at least 10% and excluding wetlands smaller
 254 than 0.01 km² underestimated emissions by at least 75% (Figure 4b).



255

256 **Figure 4.** Total annual diffusive methane emissions for focal wetlands calculated using different
 257 model assumptions. **a)** Total emissions for time-varying (blue) vs. static (orange) estimates of
 258 SWE using the 3 semi-empirical diffusive flux models described in Section 2.4. Error bars
 259 represent 5% and 95% quantiles from 1,000 model iterations. **b)** Total emissions for time-
 260 varying vs. static SWE with different minimum wetland size thresholds.

261 4 Discussion

262 We demonstrate that accounting for inundation and variable SWE in forested wetlands
 263 significantly influences calculations of diffusive methane emissions from a low-relief wetland-
 264 rich watershed. Specifically, we show that: i) previous limitations in quantifying SWE at the
 265 global scale will typically result in underestimates of methane emissions from forested wetlands;
 266 ii) as spatial resolution of wetland map products improve, accurate estimates of emissions will
 267 require improved quantification of intra-annual surface water dynamics; and iii) while fine-
 268 resolution frequent-revisit satellite imagery can help address these gaps, our ability to detect and
 269 monitor sub-canopy inundation during the late growing season is still limited. Below we discuss
 270 modeling inundation dynamics in forested wetlands and implications for the global methane
 271 budget in more detail.

272 4.1 Modeling inundation dynamics of forested wetlands using high resolution satellite 273 data

274 This study shows that it is possible to quantify intra-annual surface water dynamics in
 275 small forested wetlands (< 1,000 m²) using optical satellite data that has both fine spatial and
 276 high temporal resolution. Although classification models were able to produce inundation time
 277 series with similar patterns to the field-based time series (Figure 3), they also had consistent

278 inaccuracies, demonstrating that optical imagery alone does not accurately represent the timing
279 of surface water dynamics in forested wetlands, especially after leaf-out.

280 In fall 2017, satellite-derived SWE was overestimated compared to our field
281 measurements. We hypothesize this is attributable to unreliable classification of “permanent”
282 water features in the NWI, i.e. many of these water bodies are actually seasonal. Few alternatives
283 exist for accurate training data at spatial resolutions necessary to identify the smallest water
284 bodies, and quantitative information on hydrologic regimes is even less common. Even though
285 the NWI is very detailed and thematically rich, it has known inaccuracies in the Delmarva region
286 (Fenstermacher et al., 2014). Whereas variability in radiometry between Planet images required
287 using image-specific models in this study, data from a more consistent sensor constellation (e.g.,
288 Claverie et al., 2018) could potentially be used with a more universal classification model based
289 only on training data from time points and locations where inundation status is known with more
290 certainty. However, seasonal and event-driven patterns of suspended sediment, chlorophyll *a*,
291 and dissolved carbon (Hosen et al., 2018) could affect the optical properties of these water
292 bodies in ways that would impact model reliability .

293 In 2018, underestimates of surface water area in May and June coincided with the timing
294 of canopy leaf-out. We hypothesize that underestimates are attributable to the lag between
295 structural change in the forest canopy and the subsequent regional contraction of SWE (Figure
296 3a; Fisher et al., 2010; Lee et al., 2019). Canopy cover developing above areas that remain
297 flooded, such as on the periphery of wetland depressions, obscures surface water in optical
298 imagery. Improved methods for inundation detection under forest canopies may be possible
299 using synthetic aperture radar (SAR; Lang et al., 2008; Lang & Kasischke, 2008), combinations
300 of optical and lidar intensity data (Lang et al 2020), or improved integration with field
301 monitoring and hydrologic models that account for upland topographic depressions (Evenson et
302 al., 2018). While long-wavelength SAR sensors have been shown to be sensitive to under-canopy
303 inundation in forested wetlands (Arnesen et al., 2013; Xaypraseuth et al., 2015), these data are
304 not yet publicly available. Future satellite missions like the NASA-ISRO SAR (NISAR) mission,
305 planned for launch in 2022, will provide repeat long-wavelength SAR imagery and thus play an
306 important role in improving estimates of surface water dynamics in forested wetlands.

307 4.2 Implications for upscaling methane emissions

308 As field studies continue to document high concentrations of methane in aquatic
309 ecosystems previously overlooked as sources of emissions (Bastviken et al., 2011; Stanley et al.,
310 2015), inventory-based emission estimates of global freshwater methane fluxes have become
311 larger, more uncertain, and more at odds with top-down estimates in the global methane budget
312 (Saunois et al., 2020). Our results show that for a given set of water bodies, inventory-based
313 emission estimates can be too high in areas where inundation extent fluctuates on a seasonal
314 basis. However, non-permanent water bodies are also likely to be underrepresented in surface
315 water products or mis-classified in existing landcover products due to their small size and/or
316 obscuration by forest cover. Because the highest resolution global surface water dataset is based
317 on non-mixed 30 m pixels (Pekel et al., 2016), water bodies $< \sim 1,000 \text{ m}^2$ will be absent. At this

318 threshold, the opposing effects of inundation dynamics and missing hidden/cryptic water bodies
319 were of similar magnitude and resulted in a 10% underestimate of annual totals.

320 Understanding the source of methane is important for mitigation strategies and policies
321 aimed at reducing carbon emissions from local to global scales. Traditional upscaling approaches
322 for greenhouse gas emissions from freshwaters can be misleading for determining the dominant
323 factors driving emissions (DelSontro et al., 2018). Our results suggest that for the Greensboro
324 watershed, the water level drawdown in natural forested wetlands considerably reduces methane
325 producing areas. Where forested wetlands are lost and replaced with wetlands without a similar
326 hydroperiod, such as many wetland mitigation projects (e.g., created ponds) that result in a net
327 increase in total surface area (Dahl, 2011), methane emissions are likely to be higher. Farm
328 ponds and other small artificial water bodies have also been shown to have higher methane
329 emissions on a per-area basis (Grinham et al., 2018; Ollivier et al., 2019), and a relatively
330 constant water level only exacerbates this difference because natural wetlands have reduced
331 SWE during the warmest months when methane production rates could be the highest. The
332 ability to detect and monitor under-canopy inundation should improve with new space-borne
333 longer wavelength synthetic aperture radar (Arnesen et al., 2013; Xaypraseuth et al., 2015); as
334 these capabilities improve accurately quantifying ecosystem functions of forested wetlands will
335 also require information at high temporal resolution. Future studies may leverage these improved
336 technologies to better understand the role forested wetlands are playing in regional and global
337 methane cycles by more accurately quantifying the hydrologic processes underlying methane
338 flux to the atmosphere from inland waters.

339

340

341 **Acknowledgments, Samples, and Data**

342 Datasets used in this research are available in cited references: Holgerson and Raymond (2016),
 343 Vanderhoof and Lang (2017); Pekel et al. (2016); Jin et al (2019); USFWS (2019); and Planet
 344 (2017). Planet data are available through personal licenses to researchers for non-commercial
 345 purposes. Processing and analysis code is available online as <https://github.com/khondula/ch4est>.
 346 This work was supported by the National Socio-Environmental Synthesis Center under funding
 347 received from the National Science Foundation DBI-1639145.
 348

349 **References**

- 350 Allen, G. H., & Pavelsky, T. M. (2018). Global extent of rivers and streams. *Science*, *361*(6402), 585–588.
 351 <https://doi.org/10.1126/science.aat0636>
- 352 Arnesen, A. S., Silva, T. S. F., Hess, L. L., Novo, E. M. L. M., Rudorff, C. M., Chapman, B. D., & McDonald, K. C.
 353 (2013). Monitoring flood extent in the lower Amazon River floodplain using ALOS/PALSAR ScanSAR
 354 images. *Remote Sensing of Environment*, *130*, 51–61. <https://doi.org/10.1016/j.rse.2012.10.035>
- 355 Ator, S. W., & Denver, J. M. (2012). Estimating Contributions of Nitrate and Herbicides From Groundwater to
 356 Headwater Streams, Northern Atlantic Coastal Plain, United States ¹: ESTIMATING CONTRIBUTIONS OF
 357 NITRATE AND HERBICIDES FROM GROUNDWATER TO HEADWATER STREAMS, NORTHERN ATLANTIC
 358 COASTAL PLAIN, UNITED STATES. *JAWRA Journal of the American Water Resources Association*, *48*(6),
 359 1075–1090. <https://doi.org/10.1111/j.1752-1688.2012.00672.x>
- 360 Bastviken, D., Tranvik, L. J., Downing, J. A., Crill, P. M., & Enrich-Prast, A. (2011). Freshwater Methane
 361 Emissions Offset the Continental Carbon Sink. *Science*, *331*(6013), 50–50.
 362 <https://doi.org/10.1126/science.1196808>
- 363 Bishop, K., Buffam, I., Erlandsson, M., Fölster, J., Laudon, H., Seibert, J., & Temnerud, J. (2008). Aqua Incognita:
 364 The unknown headwaters. *Hydrological Processes*, *22*(8), 1239–1242. <https://doi.org/10.1002/hyp.7049>
- 365 Claverie, M., Ju, J., Masek, J. G., Dungan, J. L., Vermote, E. F., Roger, J.-C., Skakun, S. V., & Justice, C. (2018).
 366 The Harmonized Landsat and Sentinel-2 surface reflectance data set. *Remote Sensing of Environment*, *219*,
 367 145–161. <https://doi.org/10.1016/j.rse.2018.09.002>
- 368 Cole, J. J., Prairie, Y. T., Caraco, N. F., McDowell, W. H., Tranvik, L. J., Striegl, R. G., Duarte, C. M., Kortelainen,
 369 P., Downing, J. A., Middelburg, J. J., & Melack, J. (2007). Plumbing the Global Carbon Cycle: Integrating

- 370 Inland Waters into the Terrestrial Carbon Budget. *Ecosystems*, 10(1), 172–185.
371 <https://doi.org/10.1007/s10021-006-9013-8>
- 372 Cooley, S. W., Smith, L. C., Ryan, J. C., Pitcher, L. H., & Pavelsky, T. M. (2019). Arctic-Boreal lake dynamics
373 revealed using CubeSat imagery. *Geophysical Research Letters*. <https://doi.org/10.1029/2018GL081584>
- 374 Dahl, T. E. (2011). *Status and trends of wetlands in the conterminous United States 2004 to 2009* (p. 108). U.S.
375 Department of the Interior; Fish and Wildlife Service.
- 376 DelSontro, T., Beaulieu, J. J., & Downing, J. A. (2018). Greenhouse gas emissions from lakes and impoundments:
377 Upscaling in the face of global change: GHG emissions from lakes and impoundments. *Limnology and*
378 *Oceanography Letters*. <https://doi.org/10.1002/lol2.10073>
- 379 DeVries, B., Huang, C., Lang, M., Jones, J., Huang, W., Creed, I., & Carroll, M. (2017). Automated Quantification
380 of Surface Water Inundation in Wetlands Using Optical Satellite Imagery. *Remote Sensing*, 9(8), 807.
381 <https://doi.org/10.3390/rs9080807>
- 382 Downing, J. A., Prairie, Y. T., Cole, J. J., Duarte, C. M., Tranvik, L. J., Striegl, R. G., McDowell, W. H.,
383 Kortelainen, P., Caraco, N. F., Melack, J. M., & Middelburg, J. J. (2006). The global abundance and size
384 distribution of lakes, ponds, and impoundments. *Limnology and Oceanography*, 51(5), 2388–2397.
385 <https://doi.org/10.4319/lo.2006.51.5.2388>
- 386 Evenson, G. R., Golden, H. E., Lane, C. R., McLaughlin, D. L., & D'Amico, E. (2018). Depressional wetlands
387 affect watershed hydrological, biogeochemical, and ecological functions. *Ecological Applications*, 28(4),
388 953–966. <https://doi.org/10.1002/eap.1701>
- 389 Evenson, G. R., McLaughlin, D. L., Lane, C. R., DeVries, B., Alexander, L. C., Lang, M. W., McCarty, G. W., &
390 Sharifi, A. (2018). A watershed-scale model for depressional wetland-rich landscapes. *Journal of*
391 *Hydrology X*, 1, 100002. <https://doi.org/10.1016/j.hydroa.2018.10.002>
- 392 Fenstermacher, D. E., Rabenhorst, M. C., Lang, M. W., McCarty, G. W., & Needelman, B. A. (2014). Distribution,
393 Morphometry, and Land Use of Delmarva Bays. *Wetlands*, 34(6), 1219–1228.
394 <https://doi.org/10.1007/s13157-014-0583-5>
- 395 Fisher, T., Jordan, T., Staver, K., Gustafson, A., Koskelo, A., Fox, R., Sutton, A., Kana, T., Beckert, K., Stone, J.,
396 McCarty, G., & Lang, M. (2010). The Choptank Basin in Transition: Intensifying Agriculture, Slow

- 397 Urbanization, and Estuarine Eutrophication. In M. Kennish & H. Paerl (Eds.), *Coastal Lagoons* (Vol.
 398 20103358, pp. 135–165). CRC Press. <https://doi.org/10.1201/EBK1420088304-c7>
- 399 Griffin, C. G., McClelland, J. W., Frey, K. E., Fiske, G., & Holmes, R. M. (2018). Quantifying CDOM and DOC in
 400 major Arctic rivers during ice-free conditions using Landsat TM and ETM+ data. *Remote Sensing of*
 401 *Environment*, 209, 395–409. <https://doi.org/10.1016/j.rse.2018.02.060>
- 402 Grinham, A., Albert, S., Deering, N., Dunbabin, M., Bastviken, D., Sherman, B., Lovelock, C. E., & Evans, C. D.
 403 (2018). The importance of small artificial water bodies as sources of methane emissions in Queensland,
 404 Australia. *Hydrology and Earth System Sciences*, 22(10), 5281–5298. [https://doi.org/10.5194/hess-22-](https://doi.org/10.5194/hess-22-5281-2018)
 405 5281-2018
- 406 Halabisky, M., Moskal, L. M., Gillespie, A., & Hannam, M. (2016). Reconstructing semi-arid wetland surface water
 407 dynamics through spectral mixture analysis of a time series of Landsat satellite images (1984–2011).
 408 *Remote Sensing of Environment*, 177, 171–183. <https://doi.org/10.1016/j.rse.2016.02.040>
- 409 Hanson, P. C., Carpenter, S. R., Cardille, J. A., Coe, M. T., & Winslow, L. A. (2007). Small lakes dominate a
 410 random sample of regional lake characteristics. *Freshwater Biology*, 52(5), 814–822.
 411 <https://doi.org/10.1111/j.1365-2427.2007.01730.x>
- 412 Holgerson, M. A., & Raymond, P. A. (2016). Large contribution to inland water CO₂ and CH₄ emissions from very
 413 small ponds. *Nature Geoscience*, 9(3), 222–226. <https://doi.org/10.1038/ngeo2654>
- 414 Hosen, J. D., Armstrong, A. W., & Palmer, M. A. (2018). Dissolved organic matter variations in coastal plain
 415 wetland watersheds: The integrated role of hydrological connectivity, land use, and seasonality.
 416 *Hydrological Processes*, 32(11), 1664–1681. <https://doi.org/10.1002/hyp.11519>
- 417 Huang, C., Peng, Y., Lang, M., Yeo, I.-Y., & McCarty, G. (2014). Wetland inundation mapping and change
 418 monitoring using Landsat and airborne LiDAR data. *Remote Sensing of Environment*, 141, 231–242.
 419 <https://doi.org/10.1016/j.rse.2013.10.020>
- 420 Ji, L., Zhang, L., & Wylie, B. (2009). Analysis of Dynamic Thresholds for the Normalized Difference Water Index.
 421 *Photogrammetric Engineering & Remote Sensing*, 75(11), 1307–1317.
 422 <https://doi.org/10.14358/PERS.75.11.1307>

- 423 Jia, K., Jiang, W., Li, J., & Tang, Z. (2018). Spectral matching based on discrete particle swarm optimization: A new
424 method for terrestrial water body extraction using multi-temporal Landsat 8 images. *Remote Sensing of*
425 *Environment*, 209, 1–18. <https://doi.org/10.1016/j.rse.2018.02.012>
- 426 Jin, S., Homer, C., Yang, L., Danielson, P., Dewitz, J., Li, C., Zhu, Z., Xian, G., & Howard, D. (2019). Overall
427 Methodology Design for the United States National Land Cover Database 2016 Products. *Remote Sensing*,
428 11(24), 2971. <https://doi.org/10.3390/rs11242971>
- 429 Jones, C. N., Evenson, G. R., McLaughlin, D. L., Vanderhoof, M. K., Lang, M. W., McCarty, G. W., Golden, H. E.,
430 Lane, C. R., & Alexander, L. C. (2018). Estimating restorable wetland water storage at landscape scales.
431 *Hydrological Processes*, 32(2), 305–313. <https://doi.org/10.1002/hyp.11405>
- 432 Kuhn, C., de Matos Valerio, A., Ward, N., Loken, L., Sawakuchi, H. O., Kampel, M., Richey, J., Stadler, P.,
433 Crawford, J., Striegl, R., Vermote, E., Pahlevan, N., & Butman, D. (2019). Performance of Landsat-8 and
434 Sentinel-2 surface reflectance products for river remote sensing retrievals of chlorophyll-a and turbidity.
435 *Remote Sensing of Environment*, 224, 104–118. <https://doi.org/10.1016/j.rse.2019.01.023>
- 436 Lang, M. W., & Kasischke, E. S. (2008). Using C-Band Synthetic Aperture Radar Data to Monitor Forested
437 Wetland Hydrology in Maryland's Coastal Plain, USA. *IEEE Transactions on Geoscience and Remote*
438 *Sensing*, 46(2), 535–546. <https://doi.org/10.1109/TGRS.2007.909950>
- 439 Lang, M. W., Kasischke, E. S., Prince, S. D., & Pittman, K. W. (2008). Assessment of C-band synthetic aperture
440 radar data for mapping and monitoring Coastal Plain forested wetlands in the Mid-Atlantic Region, U.S.A.
441 *Remote Sensing of Environment*, 112(11), 4120–4130. <https://doi.org/10.1016/j.rse.2007.08.026>
- 442 Lang, M. W., Kim, V., McCarty, G. W., Li, X., Yeo, I.-Y., Huang, C., & Du, L. (2020). Improved Detection of
443 Inundation below the Forest Canopy using Normalized LiDAR Intensity Data. *Remote Sensing*, 12(4), 707.
444 <https://doi.org/10.3390/rs12040707>
- 445 Lang, McDonough, O., McCarty, G., Oesterling, R., & Wilen, B. (2012). Enhanced Detection of Wetland-Stream
446 Connectivity Using LiDAR. *Wetlands*, 32(3), 461–473. <https://doi.org/10.1007/s13157-012-0279-7>
- 447 Lee, McCarty, G. W., Moglen, G. E., Lang, M. W., Nathan Jones, C., Palmer, M., Yeo, I.-Y., Anderson, M.,
448 Sadeghi, A. M., & Rabenhorst, M. C. (2020). Seasonal drivers of geographically isolated wetland
449 hydrology in a low-gradient, Coastal Plain landscape. *Journal of Hydrology*, 583, 124608.
450 <https://doi.org/10.1016/j.jhydrol.2020.124608>

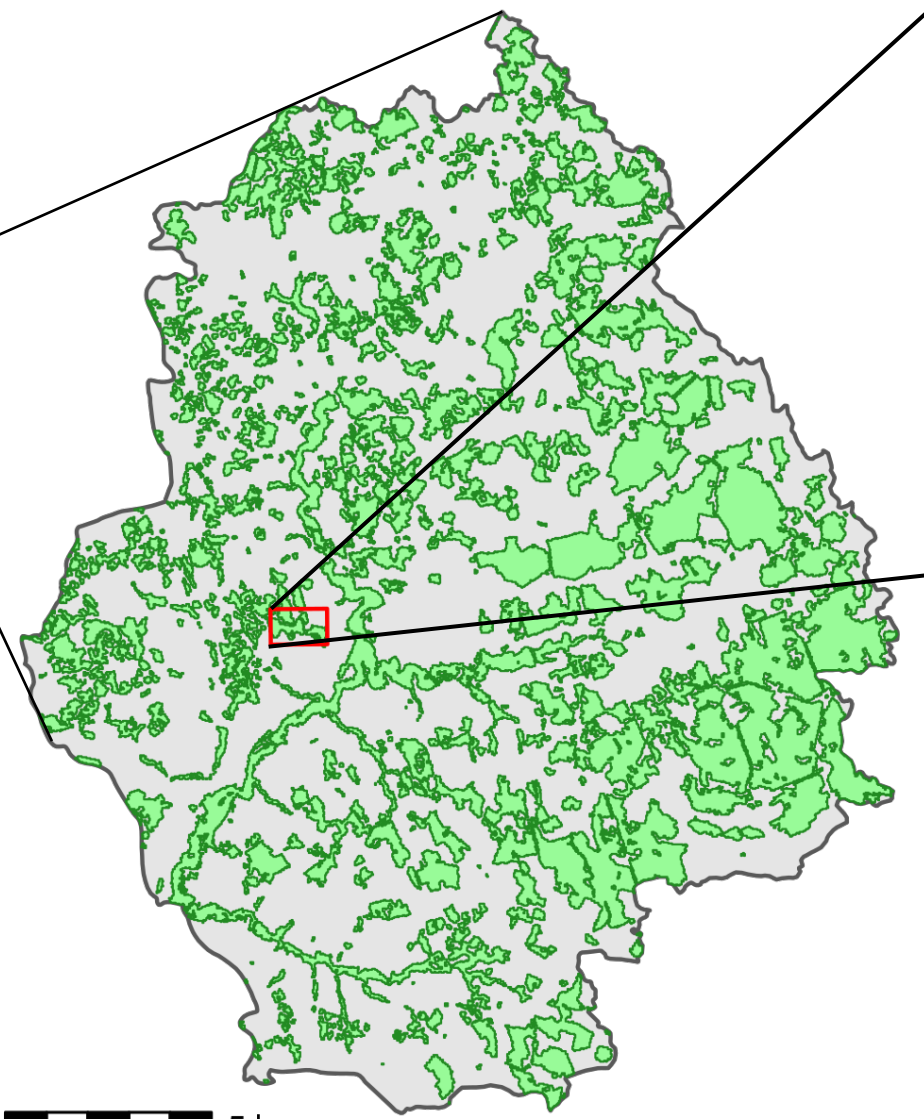
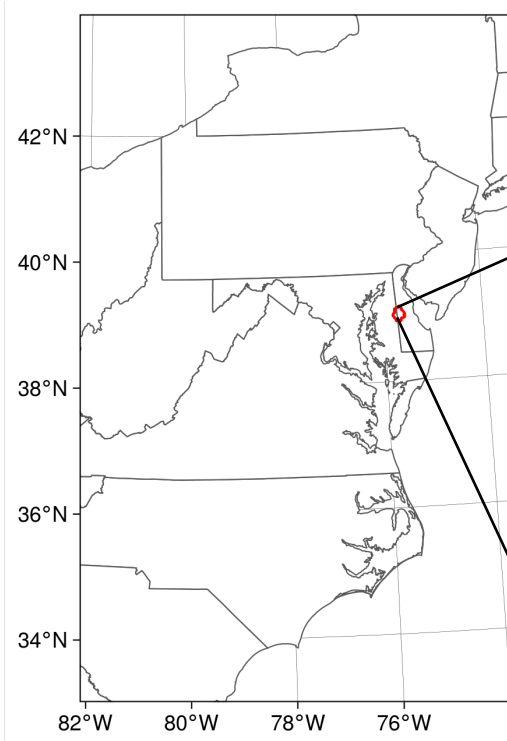
- 451 Lee, Yeo, I.-Y., Lang, M. W., McCarty, G. W., Sadeghi, A. M., Sharifi, A., Jin, H., & Liu, Y. (2019). Improving the
 452 catchment scale wetland modeling using remotely sensed data. *Environmental Modelling & Software*, *122*,
 453 104069. <https://doi.org/10.1016/j.envsoft.2017.11.001>
- 454 Lindsay, J. B. (2016). Whitebox GAT: A case study in geomorphometric analysis. *Computers & Geosciences*, *95*,
 455 75–84. <https://doi.org/10.1016/j.cageo.2016.07.003>
- 456 Lowe, W. H., & Likens, G. E. (2005). Moving Headwater Streams to the Head of the Class. *BioScience*, *55*(3), 196.
 457 [https://doi.org/10.1641/0006-3568\(2005\)055\[0196:MHSTTH\]2.0.CO;2](https://doi.org/10.1641/0006-3568(2005)055[0196:MHSTTH]2.0.CO;2)
- 458 McFeeters, S. K. (1996). The use of the Normalized Difference Water Index (NDWI) in the delineation of open
 459 water features. *International Journal of Remote Sensing*, *17*(7), 1425–1432.
 460 <https://doi.org/10.1080/01431169608948714>
- 461 Melton, J. R., Wania, R., Hodson, E. L., Poulter, B., Ringeval, B., Spahni, R., Bohn, T., Avis, C. A., Beerling, D. J.,
 462 Chen, G., Eliseev, A. V., Denisov, S. N., Hopcroft, P. O., Lettenmaier, D. P., Riley, W. J., Singarayer, J. S.,
 463 Subin, Z. M., Tian, H., Zürcher, S., ... Kaplan, J. O. (2013). Present state of global wetland extent and
 464 wetland methane modelling: Conclusions from a model inter-comparison project (WETCHIMP).
 465 *Biogeosciences*, *10*(2), 753–788. <https://doi.org/10.5194/bg-10-753-2013>
- 466 Ollivier, Q. R., Maher, D. T., Pitfield, C., & Macreadie, P. I. (2019). Punching above their weight: Large release of
 467 greenhouse gases from small agricultural dams. *Global Change Biology*, *25*(2), 721–732.
 468 <https://doi.org/10.1111/gcb.14477>
- 469 Pangala, S. R., Enrich-Prast, A., Basso, L. S., Peixoto, R. B., Bastviken, D., Hornibrook, E. R. C., Gatti, L. V.,
 470 Ribeiro, H., Calazans, L. S. B., Sakuragui, C. M., Bastos, W. R., Malm, O., Gloor, E., Miller, J. B., &
 471 Gauci, V. (2017). Large emissions from floodplain trees close the Amazon methane budget. *Nature*.
 472 <https://doi.org/10.1038/nature24639>
- 473 Parker, R. J., Boesch, H., McNorton, J., Comyn-Platt, E., Gloor, M., Wilson, C., Chipperfield, M. P., Hayman, G.
 474 D., & Bloom, A. A. (2018). Evaluating year-to-year anomalies in tropical wetland methane emissions using
 475 satellite CH₄ observations. *Remote Sensing of Environment*, *211*, 261–275.
 476 <https://doi.org/10.1016/j.rse.2018.02.011>
- 477 Pekel, J.-F., Cottam, A., Gorelick, N., & Belward, A. S. (2016). High-resolution mapping of global surface water
 478 and its long-term changes. *Nature*, *540*(7633), 418–422. <https://doi.org/10.1038/nature20584>

- 479 Phillips, P. J., & Shedlock, R. J. (1993). Hydrology and chemistry of groundwater and seasonal ponds in the Atlantic
480 Coastal Plain in Delaware, USA. *Journal of Hydrology*, *141*(1–4), 157–178. <https://doi.org/10.1016/0022->
481 [1694\(93\)90048-E](https://doi.org/10.1016/0022-1694(93)90048-E)
- 482 Planet. (2018). *Planet Imagery Product Specification: Planetscope and RapidEye*.
483 <https://www.planet.com/products/satellite->
484 [imagery/files/Planet_Combined_Imagery_Product_Specs_December2017.pdf](https://www.planet.com/products/satellite-imagery/files/Planet_Combined_Imagery_Product_Specs_December2017.pdf)
- 485 Poulter, B., Bousquet, P., Canadell, J. G., Ciais, P., Peregon, A., Saunio, M., Arora, V. K., Beerling, D. J., Brovkin,
486 V., Jones, C. D., Joos, F., Gedney, N., Ito, A., Kleinen, T., Koven, C. D., McDonald, K., Melton, J. R.,
487 Peng, C., Peng, S., ... Zhu, Q. (2017). Global wetland contribution to 2000–2012 atmospheric methane
488 growth rate dynamics. *Environmental Research Letters*, *12*(9), 094013. <https://doi.org/10.1088/1748->
489 [9326/aa8391](https://doi.org/10.1088/1748-9326/aa8391)
- 490 Raymond, P. A., Hartmann, J., Lauerwald, R., Sobek, S., McDonald, C., Hoover, M., Butman, D., Striegl, R.,
491 Mayorga, E., Humborg, C., Kortelainen, P., Dürr, H., Meybeck, M., Ciais, P., & Guth, P. (2013). Global
492 carbon dioxide emissions from inland waters. *Nature*, *503*(7476), 355–359.
493 <https://doi.org/10.1038/nature12760>
- 494 Saunio, M., Stavert, A. R., Poulter, B., Bousquet, P., Canadell, J. G., Jackson, R. B., Raymond, P. A.,
495 Dlugokencky, E. J., Houweling, S., Patra, P. K., Ciais, P., Arora, V. K., Bastviken, D., Bergamaschi, P.,
496 Blake, D. R., Brailsford, G., Bruhwiler, L., Carlson, K. M., Carrol, M., ... Zhuang, Q. (2020). The Global
497 Methane Budget 2000–2017. *Earth System Science Data*, *12*(3), 1561–1623. <https://doi.org/10.5194/essd->
498 [12-1561-2020](https://doi.org/10.5194/essd-12-1561-2020)
- 499 Seekell, D. A., Carr, J. A., Gudas, C., & Karlsson, J. (2014). Upscaling carbon dioxide emissions from lakes:
500 Upscaling CO₂ emissions from lakes. *Geophysical Research Letters*, *41*(21), 7555–7559.
501 <https://doi.org/10.1002/2014GL061824>
- 502 Stanley, E. H., Casson, N. J., Christel, S. T., Crawford, J. T., Loken, L. C., & Oliver, S. K. (2015). The ecology of
503 methane in streams and rivers: Patterns, controls, and global significance. *Ecological Monographs*.
504 <https://doi.org/10.1890/15-1027.1>

- 505 Thornton, B. F., Wik, M., & Crill, P. M. (2016). Double-counting challenges the accuracy of high-latitude methane
 506 inventories: DOUBLE-COUNTING ARCTIC METHANE. *Geophysical Research Letters*, *43*(24), 12,569-
 507 12,577. <https://doi.org/10.1002/2016GL071772>
- 508 Tranvik, L. J., Downing, J. A., Cotner, J. B., Loiselle, S. A., Striegl, R. G., Ballatore, T. J., Dillon, P., Finlay, K.,
 509 Fortino, K., Knoll, L. B., Kortelainen, P. L., Kutser, T., Larsen, Soren., Laurion, I., Leech, D. M.,
 510 McCallister, S. L., McKnight, D. M., Melack, J. M., Overholt, E., ... Weyhenmeyer, G. A. (2009). Lakes
 511 and reservoirs as regulators of carbon cycling and climate. *Limnology and Oceanography*, *54*(6part2),
 512 2298–2314. https://doi.org/10.4319/lo.2009.54.6_part_2.2298
- 513 Treat, C. C., Bloom, A. A., & Marushchak, M. E. (2018). Non-growing season methane emissions are a significant
 514 component of annual emissions across northern ecosystems. *Global Change Biology*.
 515 <https://doi.org/10.1111/gcb.14137>
- 516 Tucker, C. J. (1979). Red and photographic infrared linear combinations for monitoring vegetation. *Remote Sensing*
 517 *of Environment*, *8*(2), 127–150. [https://doi.org/10.1016/0034-4257\(79\)90013-0](https://doi.org/10.1016/0034-4257(79)90013-0)
- 518 U. S. Fish and Wildlife Service. (2019). *National Wetlands Inventory website*. U.S. Department of the Interior, Fish
 519 and Wildlife Service. <http://www.fws.gov/wetlands/>
- 520 Vanderhoof, M. K., Distler, H. E., Lang, M. W., & Alexander, L. C. (2018). The influence of data characteristics on
 521 detecting wetland/stream surface-water connections in the Delmarva Peninsula, Maryland and Delaware.
 522 *Wetlands Ecology and Management*, *26*(1), 63–86. <https://doi.org/10.1007/s11273-017-9554-y>
- 523 Vanderhoof, M. K., & Lang, M. (2017). *Data Release for the influence of data characteristics on detecting*
 524 *wetland/stream surface-water connections in the Delmarva Peninsula, Maryland and Delaware* [Data set].
 525 U.S. Geological Survey. <https://doi.org/10.5066/F70C4T8F>
- 526 Vermote, E. F., Tanre, D., Deuze, J. L., Herman, M., & Morcette, J.-J. (1997). Second Simulation of the Satellite
 527 Signal in the Solar Spectrum, 6S: An overview. *IEEE Transactions on Geoscience and Remote Sensing*,
 528 *35*(3), 675–686. <https://doi.org/10.1109/36.581987>
- 529 Wania, R., Melton, J. R., Hodson, E. L., Poulter, B., Ringeval, B., Spahni, R., Bohn, T., Avis, C. A., Chen, G.,
 530 Eliseev, A. V., Hopcroft, P. O., Riley, W. J., Subin, Z. M., Tian, H., Brovkin, V., van Bodegom, P. M.,
 531 Kleinen, T., Yu, Z. C., Singarayer, J. S., ... Kaplan, J. O. (2012). Present state of global wetland extent and
 532 wetland methane modelling: Methodology of a model intercomparison project (WETCHIMP).

- 533 *Geoscientific Model Development Discussions*, 5(4), 4071–4136. <https://doi.org/10.5194/gmdd-5-4071->
534 2012
- 535 Winslow, L. A., Zwart, J. A., Batt, R. D., Dugan, H. A., Woolway, R. I., Corman, J. R., Hanson, P. C., & Read, J. S.
536 (2016). LakeMetabolizer: An R package for estimating lake metabolism from free-water oxygen using
537 diverse statistical models. *Inland Waters*, 6(4), 622–636. <https://doi.org/10.1080/IW-6.4.883>
- 538 Wu, Q., Lane, C., & Liu, H. (2014). An Effective Method for Detecting Potential Woodland Vernal Pools Using
539 High-Resolution LiDAR Data and Aerial Imagery. *Remote Sensing*, 6(11), 11444–11467.
540 <https://doi.org/10.3390/rs61111444>
- 541 Xaypraseuth, P., Satish, R., & Chatterjee, A. (2015). NISAR spacecraft concept overview: Design challenges for a
542 proposed flagship dual-frequency SAR mission. *2015 IEEE Aerospace Conference*, 1–11.
543 <https://doi.org/10.1109/AERO.2015.7118935>
- 544 Yeo, I.-Y., Lang, M. W., Lee, S., McCarty, G. W., Sadeghi, A. M., Yetemen, O., & Huang, C. (2019). Mapping
545 landscape-level hydrological connectivity of headwater wetlands to downstream waters: A geospatial
546 modeling approach - Part 1. *Science of The Total Environment*, 653, 1546–1556.
547 <https://doi.org/10.1016/j.scitotenv.2018.11.238>
- 548 Zeileis, A., Fisher, J. C., Hornik, K., Ihaka, R., McWhite, C. D., Murrell, P., Stauffer, R., & Wilke, C. O. (2019).
549 colorspace: A Toolbox for Manipulating and Assessing Colors and Palettes. *ArXiv:1903.06490 [Cs, Stat]*.
550 <http://arxiv.org/abs/1903.06490>
- 551
552

Figure1.



5 km

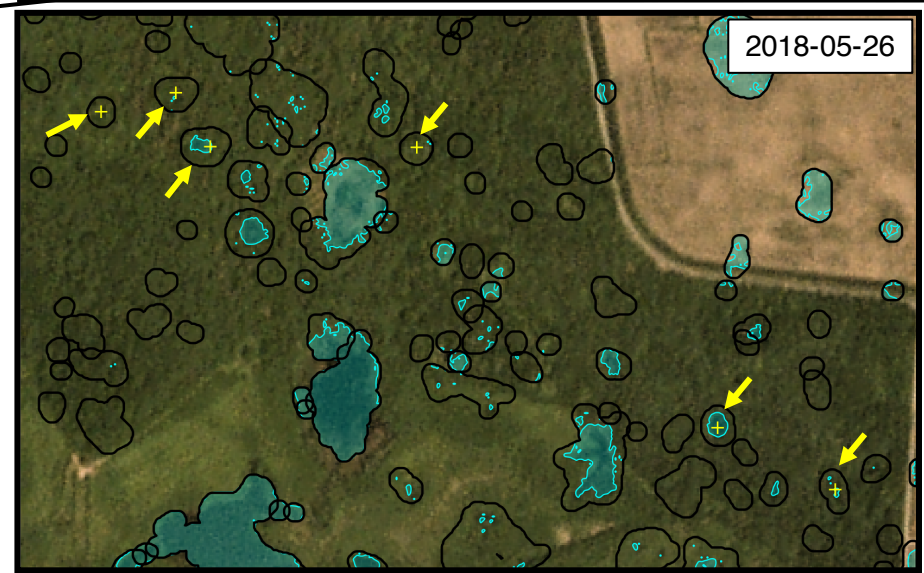
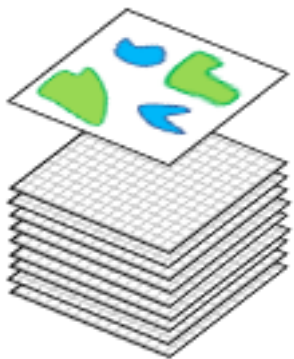


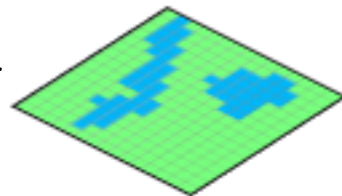
Figure2.

a) For each image

1. Calculate additional bands

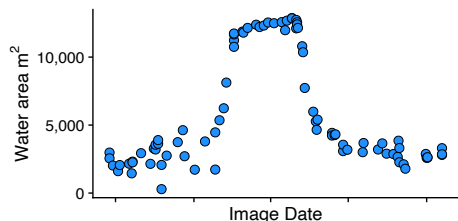
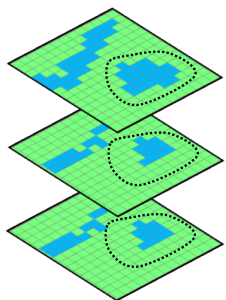


2. Train image-specific classification model

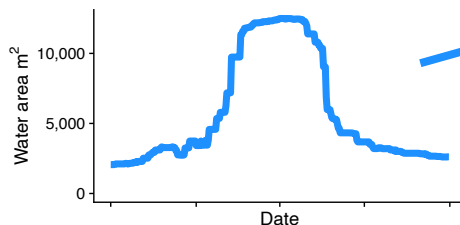


3. Apply model to predict inundation

b) For each wetland



4. Sum water area within polygon for each image

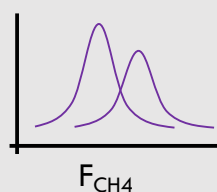


5. Calculate daily water area using moving average

c) Methane flux

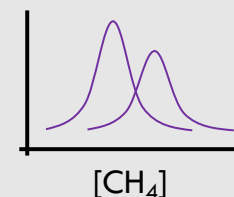
CH_4 Model A

$$\text{Flux}_{n,i} \sim f(\text{size}_n)$$

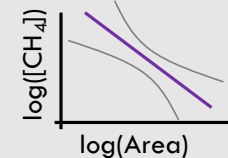


CH_4 Model B

$$\text{Flux}_{n,i} \sim f(\text{size}_n, k_{600n,i}, \text{temp}_i)$$



CH_4 Model C



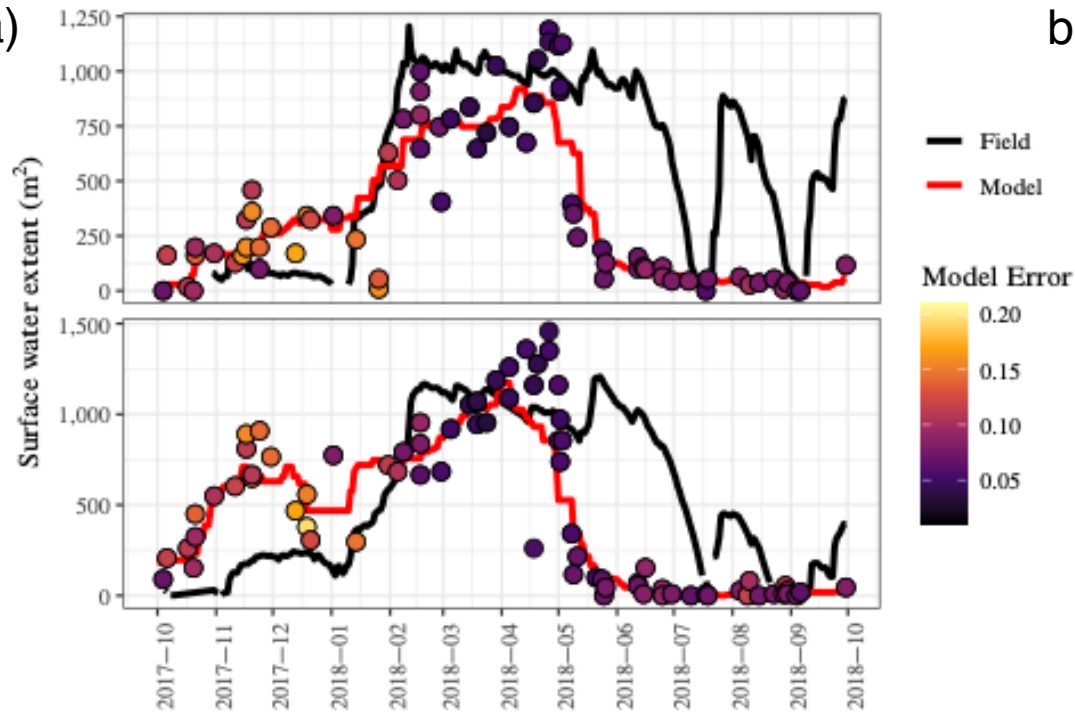
6. Sample daily wetland-specific areal flux rate from diffusive flux models

$$\text{Emissions} = \sum \sum (\text{SWE}_{n,i}) \times (\text{Flux}_{n,i})$$

7. Sum annual watershed emissions using daily surface water extent and flux rate time series for each wetland

Figure3.

a)



b)

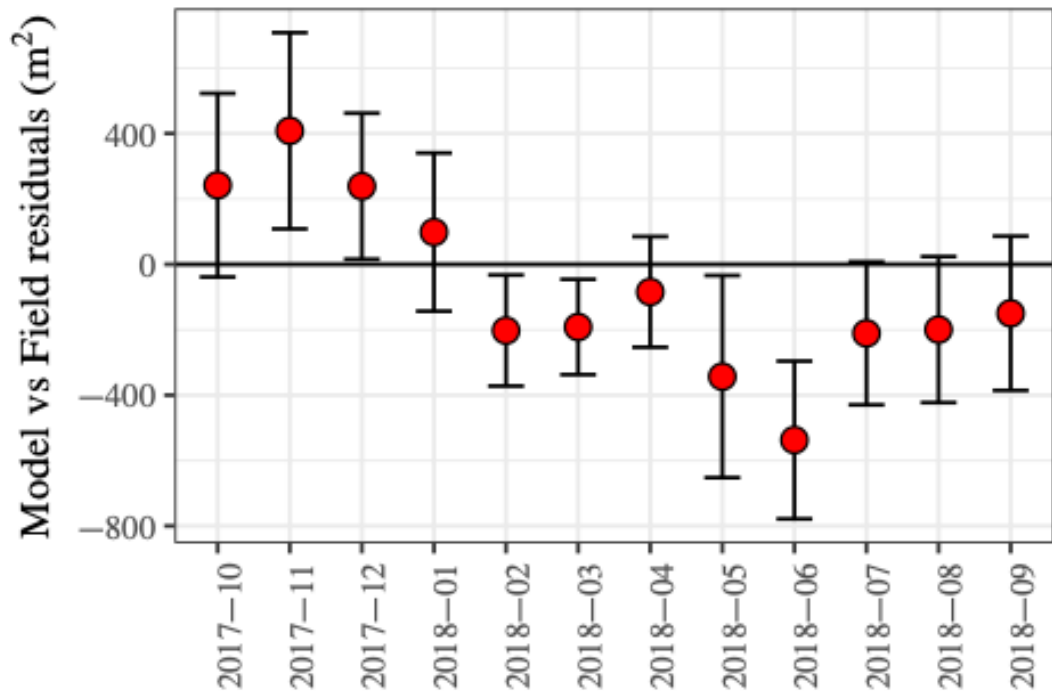
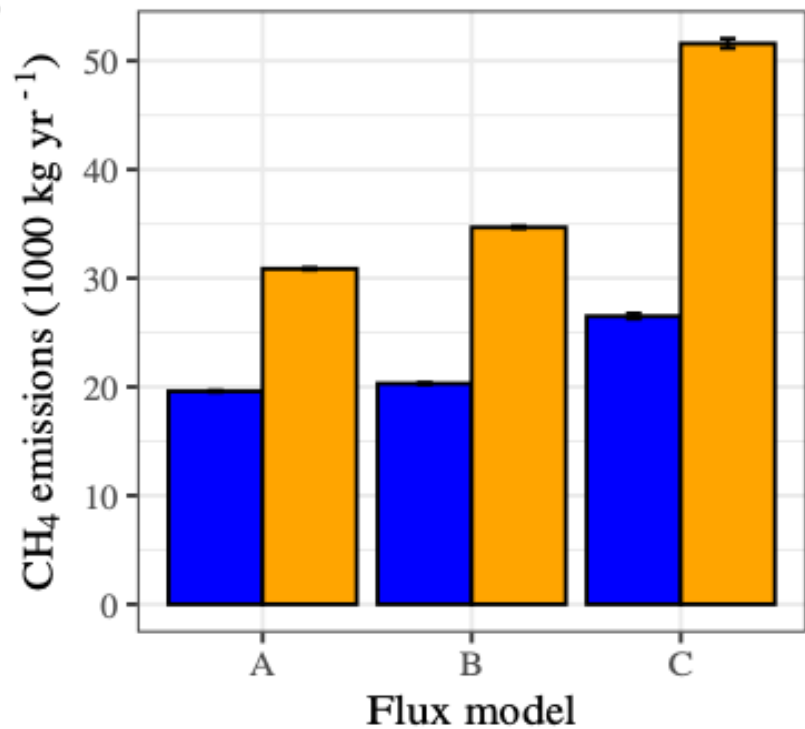


Figure4.

a)



b)

